Ab initio thermodynamics study of ambient gases reacting with amorphous carbon

Alexander Held[1,2] and Michael Moseler[1,2,3,∗]

[1]*Freiburg Materials Research Center FMF, University of Freiburg,*
Stefan-Meier-Strasse 21, 79104 Freiburg, Germany
[2]*Fraunhofer IWM, MicroTribology Center μTC,*
Woehlerstrasse 11, 79108 Freiburg, Germany
[3]*Institute of Physics, University of Freiburg,*
Hermann-Herder-Strasse 3, 79104 Freiburg, Germany

(Dated: January 31, 2019)

Abstract

Amorphous carbon (a-C) occurs as a tribologically induced phase in diamond or diamond-like carbon coatings. The interaction of ambient gases (H_2, N_2, O_2, H_2O, CO_2) with a-C of varying mass density is studied by means of ab initio thermodynamics simulations. Different scenarios such as moist air or pure gases are investigated under different pressure and temperature conditions. Equilibrium concentrations of chemisorbed and fragmented final states are found to only exhibit a minor dependence on the specific conditions of the gas phase reservoir. The differences in local structure of the a-C samples with varying mass density such as pore size, coordination and dangling bonds as well as the competition among different gas molecules for a-C atoms as reactants affect the equilibrium concentrations to a greater degree. The availability and reactivity of a-C atoms are thus found to mainly control the chemical composition of a-C interacting with ambient gases in thermodynamic equilibrium. Trends found in the analysis of chemical groups occurring in equilibrium can possibly be transferred to a more realistic non-equilibrium tribological scenario.

I. INTRODUCTION

Diamond coatings[1] and diamond-like carbon[2,3] (DLC) coatings are increasingly used in technological applications to reduce friction and wear, for instance in pumps[4,5], combustion engines[6] and transmissions[7]. Although a considerable number of experimental investigations have been performed to explore the tribological properties of these coatings (especially regarding the interaction with lubricants and ambient gases, see for instance Ref. 8), the microscopic mechanisms underlying the outstanding friction and wear behavior are still not completely understood. This is mainly due to the fact that the processes taking place at buried tribological interfaces defy any experimental in-situ observation for most tribological systems (transparent materials are an exception). Usually, an analysis is performed after tribological experiments revealing the final tribo-induced modifications of material structure and topography. Based on this post-mortem information, more or less well-founded conclusions are drawn about friction and wear mechanisms. Fortunately, in the last decades atomic scale calculations of tribological contacts have matured to such a degree that an in-situ in-silico observation of tribological processes has become a complementary technique that can help to corroborate experimental conjectures[9] or even find alternative explanations for experimental findings[10].

Classical molecular dynamics using semi-empirical atomistic force fields[11] for hydrocarbons has been extremely helpful to understand tribo-induced phase transformations in diamond and diamond-like carbon coatings subject to ultra-high vacuum conditions[12,13] or in contact with simple base oils[14]. Unfortunately, tribological systems containing many different elements currently are far too demanding for such classical molecular dynamics investigations. For that reason, quantum molecular dynamics has become an indispensable tool to study friction and wear in chemically more complex systems[10,15,16], such as hard carbon coatings in contact with environmental gases. Yet, a systematic understanding of functionalizations and phases formed in tribological contacts is currently hard to achieve due to the system sizes and time scales needed for realistic simulations[10].

In this work, we attack this problem from a different angle. Instead of simulating the kinetics and mechano-chemistry taking place during sliding of two surfaces, we look for the most likely reactions in thermodynamic equilibrium. We consider this complementary approach helpful in identifying universal reactivity trends in more time-consuming non-

equilibrium situations (with admittedly strongly reduced statistics) that is to say if certain structural motifs are observed in thermodynamic equilibrium as well as in full-fledged quantum molecular dynamics simulations, these motifs are likely to be universal. In order to demonstrate this approach we perform quantum chemical calculations of the interaction between ambient gas molecules and amorphous carbon (a-C). Elaborate experimental investigations of the final topography and the wear particles found during diamond polishing have revealed clear evidence for the formation of an a-C nano layer on the processed diamond which shows mainly sp^2 hybridization.[17,18] Recent NEXAFS analyses have detected this phase also on ultra nano-crystalline diamond[19] and on tetrahedral amorphous carbon (ta-C, H-free DLC)[20] after sliding. In these studies, the formation of functional groups involving oxygen is observed. It is yet unclear whether these groups arise from O_2 or from water. Furthermore, it is still unclear under which conditions C-O-H (hydroxyl), C-O-C (ether) or C=O (keto) groups form. Especially the incorporation of these groups into the a-C could generate an interesting interlayer with substantial influence on the tribological behavior of the carbon coatings[10].

At this point we want to recall the concept of the third-body[21,22]. In metallic tribological systems, the third body is a tribologically induced (often nano-crystalline[23]) interlayer between the two sliding partners. The composition of this interlayer is crucial for friction and wear of the tribological system. For metals, there has been a significant amount of research work dedicated to the third-body. For diamond and DLC on the other hand, the precise structure of the third-body is still elusive. Additionally, the third-body is influenced heavily by varying the ambient conditions of the experiment. For instance, a friction reducing effect of water on ta-C is reported frequently in literature, while the addition of water increases the ultra-high vacuum friction coefficient of hydrogen containing DLC (a-C:H)[8]. The precise mode of action of water is discussed controversially. It is still unclear, whether physisorption or dissociative chemisorption is determining. Interestingly, N_2 has no influence on the friction coefficient of a-C:H[8], while the friction between two a-C:H surfaces shows a strong dependence on H_2 partial pressure[24]. The mechanisms of a proposed H_2 dissociation are not resolved conclusively. Molecules involving hydroxyl groups can lead to a dramatic reduction in friction (up to superlubricity) for ta-C[25] and nanocrystalline diamond[26] and there is evidence that passivation of the surface with hydroxyl groups plays an important role[10,26,27].

Several theoretical and simulation studies focusing on the atomistic clarification of the

reactivity of carbon coatings can be found in the literature. Although first insights into possible functionalization processes have been obtained, a sufficient understanding of friction mechanisms is still missing. In an early publication Harrison *et al.*[28] have investigated ideal, partially H-terminated diamond surfaces with dangling bonds. The simulations employed an empirical interatomic force field for hydrocarbon systems. Proton transfer and cold welding of the two surfaces could be observed. Similar results have been obtained recently from density functional theory (DFT) calculations. There, the dissociation of water and H_2 was found on unterminated diamond surfaces.[29,30] It is often attempted to project the results for ideal diamond surfaces onto the wear and friction behavior of experimental diamond and DLC systems. As both have to be regarded as amorphous near the surface, the transferability of simulations involving crystalline diamond is very limited. Recent investigations of a-C layers using semi-empirical force fields[31] account for the unordered structure in experiments, yet they are limited in precision[11]. It may be possible to study the interaction with molecules containing hydroxyl groups using empirical reactive force fields[27]. However, considering the large number of fit parameters in those force fields, the quality of those simulations has to be brought into question.

In this work, we employ DFT to study bulk a-C models with periodic boundary conditions. We believe that placing gas molecules inside pores of the a-C yields a model for open pores near the a-C surface and regions that are accessible by diffusion of gas molecules through already saturated a-C layers. A systematic sampling enables us to calculate equilibrium concentrations of chemisorbed and fragmented molecules taking into account the competition among different gas phase molecules for a-C atoms as reactants. This model is certainly valid for a situation where an as-grown ta-C film is brought in contact with air yielding information of the chemical structure of a ta-C prior to tribological loading. However, as already stated above such an equilibrium model might also be useful for understanding the universal occurrence of chemical structures during sliding of hard carbon surfaces.

By varying the mass density of the a-C samples, the effect of pore size and availability of carbon atoms with different hybridization states is investigated. Equilibrium concentrations are studied as a function of temperature and pressure of the gas phase reservoir. Different compositions of the gas phase reservoir are considered in order to be able to interpret the results. Further insights are gained by identifying the chemical groups formed during the

investigated reactions. Although the scenario of thermodynamic equilibrium may be far from a tribological non-equilibrium situation during an actual asperity collision, we believe that many of our results are universal in a sense that they describe trends that should also apply to non-equilibrium scenarios, like the role of dangling bonds, the temperature dependence of hydrogen concentration and the relative concentration of carbonyl and ether groups as a function of sp content.

This work is organized as follows: In the subsections of the methods section, the generation of a-C samples, the decomposition of a-C samples into pores, details of the DFT calculations, the generation of initial and final states and the method to calculate ab initio Gibbs free energies are described. The results and discussion section is also divided into several subsections: The amorphous carbon subsection describes the analysis of a-C samples and in the thermodynamic equilibrium section, the method used to obtain the equilibrium concentrations is introduced, followed by a discussion of three important scenarios at a pressure of 10^5 Pa: moist air, equal partial pressure and pure gases. The effect of total pressure is discussed thereafter. The results and discussion section is completed by an analysis of reactants and chemical groups before all results are summarized in the conclusion.

II. METHODS

A. Generation of a-C samples

Initial a-C structures are generated by quenching from the liquid phase with a fixed mass density using classical molecular dynamics (MD) simulations. The Rebo2Scr screened reactive bond-order potential[32] as implemented in the atomistica[33] package is used to describe the carbon-carbon interaction. For a given initial mass density, particle number, and seed of the random number generator, carbon atoms are placed inside a cubic periodic simulation box at uniformly distributed random positions. The atomic positions of the initial configuration are first relaxed to a local minimum with the FIRE algorithm with residual forces below 1 eVÅ^{-1}. Afterwards, an NVT-ensemble with constant cell shape is simulated for 50 ps at 5000 K with a time step of 0.1 fs using Langevin dynamics[34] in order to equilibrate the system in the liquid state. Subsequently, the system is cooled down by performing Langevin dynamics at 300 K for 20 ps with a tenfold reduced friction coefficient. Finally,

residual forces and unit cell stress are removed by relaxing the final configuration to a local minimum.

B. Pore decomposition

For the analysis of the pore size distribution of the a-C samples, carbon atoms are treated as spheres with the covalent radius (0.76 Å)[35]. We then define a distance map $d(\boldsymbol{r})$ assigning to each point $\boldsymbol{r}$ in the simulation cell U the distance to the closest carbon sphere (see Fig. SM1 a) of the Supplemental Material[36]). The employed numerical resolution for the distance map is 0.1 Å. For a given test radius R we decompose the set of all points $U_R = \{\boldsymbol{r} \in U | d(\boldsymbol{r}) \geq R\}$ into path-connected components which we denote as pores. It then holds that for every two points in a pore, there exists a continuous path connecting the two points such that a test sphere with radius R can move along the path without colliding with the carbon spheres. And such a test sphere cannot move without collision between any two distinct pores. The decomposition into connected components is realized using standard image processing algorithms[37]: For a given test radius, a binary field is created by assigning to each spatial position whether a sphere with the test radius would fit based on the distance map (see Fig. SM1 b)). Connected components of the binary field are determined with a connectivity kernel taking into account neighboring voxels within a distance of $1.01 \cdot \sqrt{3} \cdot 0.1$ Å, which corresponds to all direct and diagonal neighbors for a cubic simulation cell (see Fig. SM1 c)). The additional factor 1.01 serves to obtain a similar connectivity kernel for cells which are not perfectly cubic after stress relaxation. Periodic boundary conditions are taken into account for each image processing step.

C. DFT calculations

Simulation details for the DFT calculations are as follows: Spin-polarized density functional theory calculations are performed using the VASP[38–41] software. The exchange-correlation functional is approximated using the PBE[42,43] functional. The projector augmented-wave method with the scalar-relativistic frozen-core approximation is used to solve the Kohn-Sham equations.[44–46] Pseudo wave functions are expanded in a plane wave basis set with an energy cutoff of 600 eV. Γ-point calculations are performed for the amorphous samples. The

6

[He] electronic states are considered as frozen-core states for C, N and O. Van der Waals interactions are treated explicitly by the Tkatchenko and Scheffler method with periodic Ewald correction.[47,48] Ionic and cell relaxations are performed using the FIRE[49] algorithm as implemented in the atomic simulation environment package (ASE)[50]. All systems are relaxed until generalized forces fall below 0.02 eVÅ^{-1}. The scaling of the unit cell forces is tuned such that the cell relaxation proceeded on similar time scales (number of relaxation steps) as the ionic relaxation with typical residual stress tensor components below 0.5 kbar. For the DFT relaxation of pristine a-C structures, initial magnetic moments of 1 μ_B per carbon atom in a ferromagnetic ordering are used and the total magnetization is allowed to relax. Vibrational frequencies of molecules and molecular fragments are determined using the finite displacement method with two displacements per degree of freedom and a step size of 0.015 Å as implemented in VASP. Local magnetic moments are determined using the PAW projection scheme as implemented in VASP.

D. Generation of initial and final states

Each of the five molecules H_2, N_2, O_2, H_2O, and CO_2 is relaxed in cubic simulation cells with a volume corresponding to a carbon mass density of 2.2 gcm^{-3} using DFT, yielding the gas phase initial states. Forces and unit cell stress of a particular a-C sample under consideration are relaxed at the DFT level of theory, yielding the a-C initial state. Then configurations of molecules near the walls of a-C pores are created as follows: For every given molecule M, pores of the DFT-relaxed a-C structure were identified as connected components with a test radius R_M given as

$$R_M = \max_{a \in M} \left(\|\boldsymbol{r}_a\| + R_a \right) \tag{1}$$

with $\boldsymbol{r}_a$ the position of atom a in M with the center of mass as the origin and R_a the covalent radius[50] of atom a. Subsequently, initial adsorption sites are identified as all molecule/a-C carbon atom/pore combinations (M, C, P) fulfilling the following condition: For the pore P in the pore decomposition with radius R_M there exists a point $\boldsymbol{r} \in P$, such that C is the closest a-C carbon atom to $\boldsymbol{r}$ and $\boldsymbol{r}$ is the closest point to C inside P. For each of those sites, an initial structure is created by placing the center of mass of M at such a point $\boldsymbol{r}$. Or in other words: The connected components are further split into Voronoi volumina[37] (see

7

Fig. SM1 d)) and reduced to a single point r which is closest to the corresponding carbon atom (see Fig. SM1 e)). After placing the molecule at r, it is rotated around its center of mass, such that the distance between the atom C and an atom of the molecule (hydrogen in the case of H_2O and oxygen in the case of CO_2) is minimized. All those configurations are then relaxed using DFT (stress and forces) to yield the collection of our reaction final states. For the relaxation of final states, initial magnetic moments of the carbon atoms are chosen to be the slightly up-scaled local magnetic moments from the corresponding a-C calculation. For the initial magnetic moments of the atoms of M, we use 1.3 μ_B per atom for O_2 and 0.2 μ_B per atom else. We again allow for a relaxation of the total magnetization during the simulation as in the a-C case. Thus spin is not necessarily conserved in our calculations. We focus on the scenario of thermodynamic equilibrium and thus we allow also "spin-forbidden" reactions with potentially slow kinetics[51]. Furthermore, a-C samples of realistic size might serve as a spin reservoir which we cannot model with our small systems. Thus we decided to relax the total magnetic moment in our calculations. The whole procedure is repeated for all a-C samples under consideration.

For the identification of the nature of the final state and the chemical groups formed by its fragments, we apply the following procedure: We assign to each product X a connectivity graph of the fragments using a distance based nearest neighbor analysis including first a-C neighbors. The bond length cutoffs have been taken as the upper quartile of experimentally observed bond-lengths[52] scaled by a factor of 1.15 to be consistent with the cutoff of 1.85 Å for C-C used in the coordination analysis in section III A. For H-H, the bond length of the hydrogen dimer scaled by 1.15 was used. The cutoffs are listed in Table SM1 of the Supplemental Material[36]. As a sanity check, we have plotted the cutoffs together with a bond length histogram of all investigated structures in Fig. SM4 of the Supplemental Material[36]. In all cases, the cutoffs are located to the right of the first cluster in the histogram and separate it from the second cluster if it exists. We have classified the fragments into three main groups by analyzing whether M^* is isolated in the pore (the fragment connectivity graph is isomorphic to the gas phase graph), chemisorbed on the pore wall (M^* is not isolated and the M^* subgraph without any a-C atoms is isomorphic to the gas phase graph) or fragmented (else). Chemical groups were identified as graph equivalence classes (graph modulo reordering/relabeling of nodes) of the connected components of the connectivity graph of each final state. The graph equivalence class corresponds 1:1 to a chemical group. That

is to say only the distance-cutoff based connectivity analysis was used to detect chemical groups (not employing bond angle or electronic structure information).

E.   Gibbs free energies

For calculating Gibbs free energy changes needed for the equilibrium concentrations of fragmented and/or chemisorbed gas molecules in a-C pores, we employ ab initio thermodynamics[50,53,54]: The change in Gibbs free energy from the molecule M in the gas phase and the pristine a-C to the molecule having reacted with the a-C to form final state X can then be expressed as

$$\Delta G = G(X) + G((N_{\mathrm{M}} - 1) \cdot M) - G(\text{a-C}) - G(N_{\mathrm{M}} \cdot M) \tag{2}$$

where N_{M} is the number of gas molecules in the reservoir and the Gibbs free energies are calculated according to

$$G = U - TS + pV = E_{\mathrm{DFT}} - TS_{\mathrm{el}} + A_{\mathrm{TRV}} + pV. \tag{3}$$

Here U is the internal energy and S the entropy. E_{DFT} denotes the total ground state energy as obtained from a relaxed density functional theory calculation including the potential energy of the nuclei. S_{el} is the electronic entropy and A_{TRV} the Helmholtz free energy due to translation, rotation and vibration of the nuclei.

We neglect the electronic entropy of the solid phases a-C and X due to their non-metallic character. Furthermore we make the usual assumption that the change in A_{TRV} from a-C to X is dominated by the vibration modes of the M fragments M*, liberating us from the need to perform expensive phonon calculations.[50] In summary, the Gibbs free energy change of such a process can be expressed as

$$\Delta G = E_{\mathrm{DFT}}(X) - E_{\mathrm{DFT}}(\text{a-C}) + A_{\mathrm{vib}}(M^*) + p(V(X) - V(\text{a-C})) - \mu_{\mathrm{M}} \tag{4}$$

with μ_{M} the chemical potential of M in the gas reservoir. For the latter, we assume an ideal gas mixture for given partial pressures (or molar ratios) of the individual molecules. The chemical potential μ_{M} is then obtained from the gas phase DFT calculation of M including vibrational analysis and tabulated values of the geometry (atom, linear, nonlinear), symmetry number[55] and ground state spin degeneracy of M.[50] For O_2, the triplet

state was employed. For water, the partial pressure is adapted to keep water vapor in equilibrium with the liquid phase whenever it exists:

$$\mu_{H_2O}(p, T) = \min\left\{\mu_{H_2O(l)}^{\text{exp}}(p, T), \ \mu_{H_2O(g)}^{\text{DFT}}(pN_{H_2O}/N_{\text{gas}}, T)\right\} \tag{5}$$

Here $\mu_{H_2O(l)}^{\text{exp}}(p, T)$ is the tabulated experimental[55] chemical potential of liquid water at pressure p and temperature T, $\mu_{H_2O(g)}^{\text{DFT}}(p, T)$ is the chemical potential of a pure ideal H_2O gas from our DFT calculations at pressure p and temperature T and N_{H_2O}/N_{gas} is the fraction of water molecules in the ideal gas mixture when no liquid water can exist. The experimental values for the chemical potential have been shifted in a way that the experimental ideal gas values[55] match our DFT ideal gas values at $p = 10^5$ Pa, $T = 300$ K in order to eliminate an arbitrary offset. The pressure and temperature dependence of the ideal gas chemical potentials are in excellent agreement between DFT and experiment, such that the switching between experimental and DFT values is smooth.

The $E_{\text{DFT}}(\text{a-C})$, $V(\text{a-C})$, $E_{\text{DFT}}(\text{X})$ and $V(\text{X})$ values are extracted directly from our a-C and X DFT simulations. We assume that differences in E_{DFT} and V between a-C and X are independent of the external (hydrostatic) pressure on the simulation cell as both systems should react similarly to external pressure leading to a cancellation in the differences. All relaxations have been performed at zero external pressure. In order to test this assumption we have re-relaxed one of the low mass density a-C samples and a randomly chosen final state that originated from this sample with an external pressure of 1 GPa instead of zero pressure. The change of the energy difference between a-C and X and the change of the pressure-volume work of the solid phase at 1 GPa were both about 1 meV. Thus this assumption is justified. $A_{\text{vib}}(M^*)$ is evaluated by fixing the carbon atoms of X and performing a vibrational analysis with only the M^* degrees of freedom with real-valued vibrational frequencies in the harmonic approximation. The ASE package was used to evaluate equation (4).

III. RESULTS AND DISCUSSION

A. Amorphous carbon samples

For each configuration (N, ρ_{in}), eight different samples are generated by changing the seed of the pseudo random number generator as described in section II A. The number of carbon atoms N was varied between 64, 128 and 512. The initial mass density ρ_{in} was varied from

TABLE I. Mass densities, coordination ratios and associated hybridization states for the four virtual pieces of a-C examined at the DFT level of theory.

virtual sample	ρ (gcm^{-3})	α_c (%)		
		2NN (sp)	3NN (sp^2)	4NN (sp^3)
1	1.84 ± 0.03	20 ± 2	74 ± 3	6.2 ± 0.5
2	2.41 ± 0.01	2.8 ± 0.4	83 ± 2	14 ± 2
3	3.01 ± 0.03	0.2 ± 0.2	38 ± 3	62 ± 3
4	3.26 ± 0.01	0 ± 0	13 ± 1	87 ± 1

1.6 gcm^{-3} to 3.6 gcm^{-3} in steps of 0.2 gcm^{-3}. For further analysis, all samples of a given configuration are subsumed into a single virtual sample with mass density

$$\rho = \frac{8N m_\mathrm{C}}{\sum_{i=1}^{8} V_i} = \frac{N_\mathrm{S} m_\mathrm{C}}{V_\mathrm{S}} \tag{6}$$

where m_C is the mass of a carbon atom, V_i are the volumes of the relaxed simulation cells, V_S is the total volume of the virtual sample and $N_\mathrm{S} = 8N$ is the total number of carbon atoms in the virtual sample.

The last relaxation typically changes the mass density of the system due to the cell relaxation. The magnitude of this effect is shown in Fig. 1 for $N = 128$. At low to medium densities, the samples contract during relaxation, while the samples expand for $\rho_\mathrm{in} > 3$ gcm^{-3}. Relaxing the structures further at the DFT level results in slightly more compact structures compared to the Rebo2Scr results. This can be attributed to slightly reduced equilibrium bond lengths in the DFT calculations. For the DFT calculations, only configurations with $N = 128$ and initial mass densities of 1.6, 2.2, 2.8 and 3.4 gcm^{-3} are analyzed. The final DFT-relaxed samples cover mass densities ranging between 1.84 gcm^{-3} and 3.26 gcm^{-3}. Their properties are listed in Table I.

An analysis of the coordination numbers of the Rebo2Scr-relaxed samples for different particle numbers is shown in Fig. 2. The values for the DFT-relaxed samples with 128 atoms are also shown. In order to get a rough estimate for the hybridization states of the a-C atoms, we have identified two nearest neighbors with sp, three nearest neighbors with sp^2 and four nearest neighbors with sp^3 hybridization. The coordination ratio for n nearest
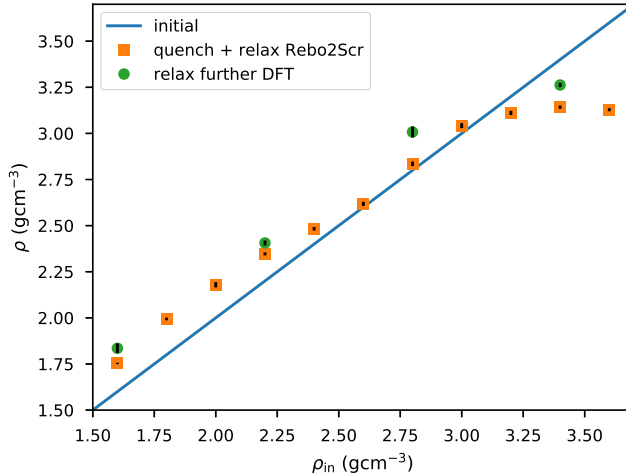
FIG. 1. (Color online) Mass density for the a-C_{128} samples after quenching and relaxing with the Rebo2Scr potential and further relaxing with DFT as a function of initial mass density. ρ_{in} denotes the initial and ρ the final mass density after quenching and relaxation with the classical force field Rebo2Scr (orange squares) as well as after further relaxation using DFT (green circles). Error bars (black vertical lines) indicate the absolute error of $\rho(\{V_i\})$ assuming that the absolute error of V_i is the sample standard deviation of $\{V_i\}$.

neighbors (NN) and a given configuration (N, ρ_{in}) is defined as

$$\alpha_c(n) = \frac{1}{N_S} \sum_{i=1}^{8} \sum_{j=1}^{N} \delta_{n,\text{coord}(i,j)} \tag{7}$$

where $\text{coord}(i, j)$ is the coordination number of atom j in sample i for the given configuration and we have used a cutoff of 1.85 Å for counting nearest neighbors.[32] In order to estimate the uncertainty of $\alpha_c(n)$, we have used the estimated standard deviation of the mean of the set $\left\{ \frac{1}{N} \sum_{j=1}^{N} \delta_{n,\text{coord}(i,j)} \right\}$.

Up to a mass density of 2.6 gcm^{-3}, the a-C consists predominantly of 3-fold coordinated (sp^2 hybridized) atoms. For higher densities an increasing fraction of sp^3 carbon is observed. For the highest investigated densities, 4-fold coordinated atoms dominate with $\alpha_c \approx 85\%$, which indicates that the employed reactive potential leads to realistic a-C structures for densities that are characteristic for tetrahedral amorphous carbons.[32,56] For ρ below 2.5 gcm^{-3}, twofold coordinated (sp hybridized) atoms begin to show up. As can be seen in Fig. 2, there is no significant difference in the coordination ratios between the a-C_{128} and a-C_{512} samples. The a-C_{64} samples show minor deviations in the low density regime, which can be attributed
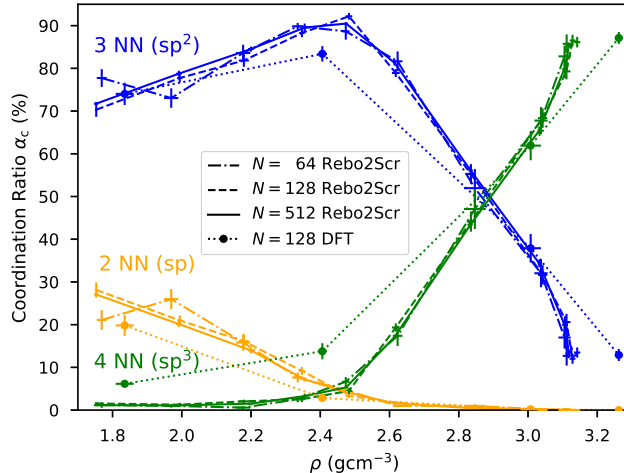
FIG. 2. (Color online) Coordination ratio for 2, 3 and 4 nearest neighbors (NN) of the Rebo2Scr-relaxed and DFT-relaxed samples as a function of the final mass density ρ for different particle numbers. Error bars for ρ as in Fig. 1. Error bars for α_c as explained in main text.

to the altered pore size distribution due to the smaller simulation boxes. The DFT-relaxed samples show qualitatively the same trends with the major difference that the sp^3 fraction ($\alpha_c(4)$) is slightly higher in the low mass density regime. The coordination ratios for the DFT-relaxed structures are listed in Table I.

In a last step, we have performed a pore decomposition of the samples. The technical details are described in depth in section II B. Figure 3 displays the radius of the largest pore R_{max} as a function of the mass density for the Rebo2Scr- and DFT-relaxed samples along with the radii R_M of the molecules as defined in equation (1). For the lower mass densities, samples with more carbon atoms show larger values of R_{max}. This is expected, as the maximum pore size should increase with sample volume. For all but the highest mass densities of the DFT-relaxed samples, there exist pores big enough to accommodate any of the molecules except CO_2. For the highest mass density, only H_2 fits into the DFT-relaxed samples and CO_2 only fits in the lowest density samples. A detailed analysis of the pore decomposition is found in the Supplemental Material[36].

Finally, we analyze the local magnetic moments of the carbon atoms in the DFT simulations in order to get an estimate for the occurrence of dangling bonds. In order to test whether dangling bonds can be detected by looking at the local magnetic moments, we perform DFT simulations for two molecules representing model systems for a dangling bond on
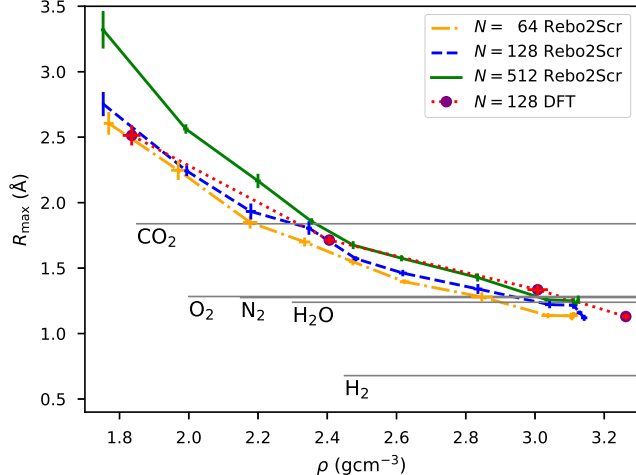
FIG. 3. (Color online) Radius of the largest test sphere fitting into the a-C as a function of mass density. Horizontal lines show the radii R_M of the molecules.

a two-fold and three-fold coordinated carbon atom. Here, the same computational parameters are used as for the a-C samples. The two-fold coordinated model system is assembled from a propyne (CH-C-CH$_3$) molecule and an allene (CH$_2$-C-CH$_2$) molecule to yield a CH$_2$-C-CH$_3$ molecule as shown in Fig. SM3 a) of the Supplemental Material[36]. For the three-fold coordinated model system we use a tert-butyl radical as shown in Fig. SM3 b) (Supplemental Material[36]). The structures are obtained from ChemSpider[57]. The local magnetic moments of the central carbon atoms are about 0.5 μ_B in the two-fold and 0.4 μ_B in the three-fold coordinated case. All other atoms exhibit absolute values of the local magnetic moments below 0.1 μ_B. This is consistent with DFT simulations of bulk magnetic carbon systems from the literature where a local magnetic moment of 0.3 μ_B was found for dangling bonds on three-fold coordinated atoms.[58]

Based on these findings, we have chosen a threshold for the absolute value of the local magnetic moment of 0.3 μ_B for qualifying a carbon atom to have a dangling bond. A histogram of the absolute values of the local magnetic moments of the a-C samples is shown in Fig. 4. Table II lists the occurrence of dangling bonds at atoms labeled as 2-fold or 3-fold coordinated for the different samples. For the virtual sample with lowest mass density, two thirds of all dangling bonds occur at 2-fold coordinated atoms, one third occurs at 3-fold coordinated atoms and in total, 1.5 % of all carbon atoms have a dangling bond. The virtual sample with $\rho = 2.41$ gcm^{-3} exhibits almost no dangling bonds. We are however not sure
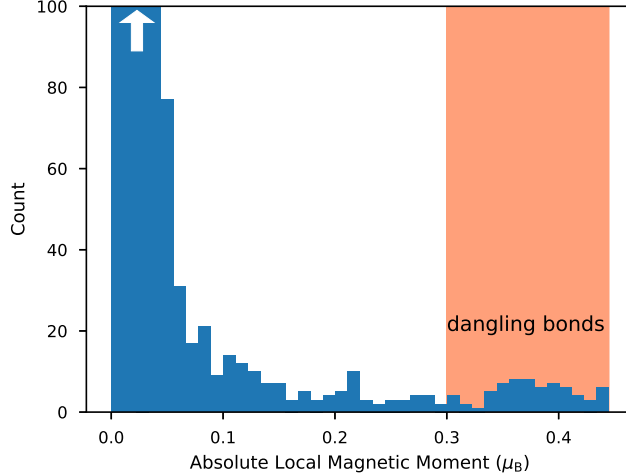
14

FIG. 4. (Color online) Histogram of the absolute values of the local magnetic moments of the carbon atoms in the a-C samples from the DFT simulations. Shaded region: carbon atoms qualified as having a dangling bond. White arrow: count exceeds visible region of plot.

TABLE II. Ratios of dangling bonds for the virtual a-C samples. N_{db}: number of carbon atoms with a dangling bond. N_{n-fold}: number of n-fold coordinated carbon atoms. N_S: total number of carbon atoms in the virtual sample.

virtual	2-fold coord. (%)		3-fold coord. (%)		total (%)
sample	$\frac{N_{db}}{N_{2\text{-fold}}}$	$\frac{N_{db}}{N_S}$	$\frac{N_{db}}{N_{3\text{-fold}}}$	$\frac{N_{db}}{N_S}$	$\frac{N_{db}}{N_S}$
1	4.9	1.0	0.7	0.5	1.5
2	0.0	0.0	0.1	0.1	0.1
3	0.0	0.0	4.9	1.9	1.9
4	-	0.0	25.0	3.2	3.2

whether this is due to an insufficient sampling size or due to the local structure at this mass density. For the two samples with highest mass density, all dangling bonds occur at 2-fold coordinated atoms. In the sample with highest mass density, 25 % of the 2-fold coordinated atoms and 3.2 % of all atoms have a dangling bond.

Further investigation of the local environment of selected carbon atoms showed that there are cases where a 3-fold coordinated atom is completely surrounded by 4-fold coordinated atoms as in Fig. SM3 b) (Supplemental Material[36]) but does not exhibit a dangling bond according to the local magnetic moment. We also found cases where 3-fold coordinated atoms
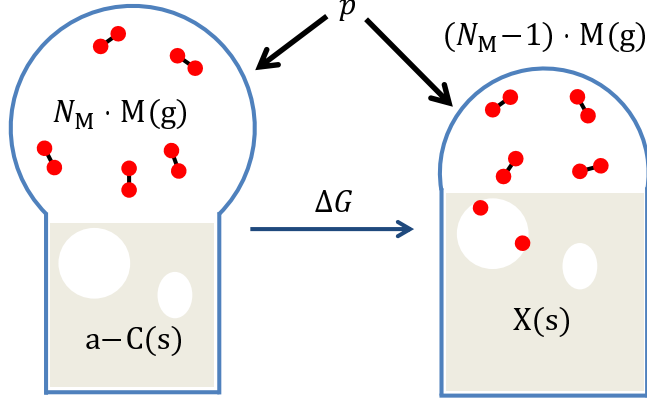
FIG. 5. (Color online) Schematic illustration of the transfer of a molecule M from the gas phase into an a-C pore undergoing fragmentation and adsorption resulting in the product X in the NpT-ensemble. Here, (g) denotes gas phase and (s) solid state species.

showed a dangling bond according to the local magnetic moment but were not completely surrounded by 4-fold coordinated atoms. It is therefore not possible to detect the location of dangling bonds from the simple distance based coordination analysis alone. We thus rely on the local magnetic moment to assign dangling bonds for further analysis. It is now interesting to see whether there is a difference in reactivity of a-C atoms when interacting with environmental gas molecules based on coordination (hybridization state) and occurrence of dangling bonds.

B. Thermodynamic equilibrium

We now want to address the ability of the a-C pores to accommodate ambient gas molecules or fragments thereof in the scenario of thermodynamic equilibrium. For this purpose, we study reactions of the type

$$N_{\mathrm{M}} \cdot \mathrm{M(g)} + \text{a-C(s)} \longrightarrow (N_{\mathrm{M}} - 1) \cdot \mathrm{M(g)} + \mathrm{X(s)} \tag{8}$$
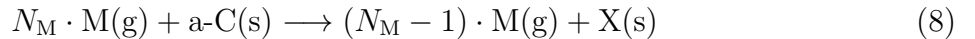
with N_{M} the number of ambient gas molecules M (H_2, N_2, O_2, H_2O, CO_2) in the reservoir and X a possible reaction product of M interacting with the a-C inside a pore. We employ an NpT-ensemble and calculate the changes in Gibbs free energy of such reactions using ab initio methods as described in detail in sections II D and II E. This scenario is illustrated schematically in Fig. 5.

For the analysis of the concentrations of chemisorbed or fragmented molecules shown later, it turns out to be crucial that every initial adsorption site (M, C, P) (see section II D) of the a-C structures is sampled. Our first attempt was to sample each of the a-C structures only partially and extrapolate results to a complete sampling. However, the extrapolation procedure turned out to be error-prone, as the competition between different molecules or molecular fragments for bonds to the same a-C carbon atoms is only reproduced correctly for a complete sampling of all initial adsorption sites. As such a sampling would be computationally too demanding when applied to all the DFT-relaxed structures, we have decided to select for each mass density only the a-C structure which most closely resembles the features of the combined virtual sample. For this purpose, we use the number concentrations of carbon atoms without dangling bonds and two, three and four nearest neighbors as well as the number concentrations of carbon atoms with a dangling bond and two and three nearest neighbors as a feature vector of length five to describe the individual and the virtual samples. For each initial mass density, we whiten the feature vectors of the individual a-C samples by dividing every component of the vectors by the according standard deviation of the feature, dropping all components with zero standard deviation (possibly reducing the lengths of the feature vectors). We then apply the same whitening operator to the feature vector of the combined virtual sample and select the individual sample with the smallest Euclidean feature vector distance. Table SM2 (Supplemental Material[36]) lists the feature vectors and mass densities of the virtual samples and the selected best representatives. In all four cases, the selected representatives closely resemble the combined virtual sample. During further analysis, it turned out that the best representative for the third mass density was an outlier regarding H_2-concentration. We thus decided to choose the second best representative for this mass density, which showed H_2-concentrations in better agreement with the other samples. The according feature vector is also listed in Table SM2 of the Supplemental Material[36]. The selected representative a-C structures are shown in Figure SM5 (Supplemental Material[36])

In total, we have analyzed 1603 possible final states X (705 for H_2, 277 for N_2, 273 for O_2, 288 for H_2O and 60 for CO_2). Out of the 1603 investigated cases, there were 709 isolated, 660 fragmented and 234 chemisorbed final states (see section II D). In all cases where the molecules fragmented, all fragments were found to be chemisorbed on a pore wall.

In order to estimate the magnitude of the different contributions to the Gibbs free energy

change, we rewrite ΔG from equation (4) as

$$\Delta G = \underbrace{E_{\mathrm{DFT}}(\mathrm{X}) - E_{\mathrm{DFT}}(\text{a-C}) - E_{\mathrm{DFT}}(\mathrm{M})}_{\Delta E_{\mathrm{DFT}}}$$
$$+ \underbrace{p\left(V(\mathrm{X}) - V(\text{a-C})\right) - k_{\mathrm{B}}T}_{p\Delta V}$$
$$+ \underbrace{A_{\mathrm{vib}}(\mathrm{M}^*) - (\mu_{\mathrm{M}} - E_{\mathrm{DFT}}(\mathrm{M}) - k_{\mathrm{B}}T)}_{\Delta G_{\mathrm{r}}}$$
$$= \Delta E_{\mathrm{DFT}} + p\Delta V + \Delta G_{\mathrm{r}} \tag{9}$$

with ΔE_{DFT} the energy contribution from the DFT simulations and $p\Delta V$ the pressure-volume work of the solid phase and the gas phase reservoir (see Fig. 5). The remaining term ΔG_{r} includes the vibrational part of the Helmholtz free energy $A_{\mathrm{vib}}(\mathrm{M}^*)$ of the molecule fragments in X, the vibrational, translational and rotational part of the Helmholtz free energy $A_{\mathrm{TRV}}(\mathrm{M})$ of M in the gas phase and the electronic entropy contribution of M in the gas phase. As the three contributions ΔE_{DFT}, $p\Delta V$ and ΔG_{r} may have different signs, we define a measure for the magnitude of the contributions as

$$C(x) = \frac{|x|}{|\Delta E_{\mathrm{DFT}}| + |p\Delta V| + |\Delta G_{\mathrm{r}}|}, \qquad x = \Delta E_{\mathrm{DFT}}, \ p\Delta V, \ \Delta G_{\mathrm{r}}. \tag{10}$$

Histograms of C are shown in Fig. 6 (a) – (c) for $p = 1$ GPa, $T = 300$ K and an imaginary ideal gas mixture with equal partial pressures of $p/5$ for each of the five molecules. It can be seen that the DFT energy is dominating in many cases. Except for some rare cases, the pressure-volume work is negligible even at $p = 1$ GPa. The remaining term ΔG_{r} including the vibration analysis makes an important contribution in many cases and even dominates in some cases as can be seen in Fig. 6 (b). For the same conditions, a histogram of the ΔG values is shown in Fig. 6 (d). Some final states are more favorable than the separate a-C + M system by several eV. Investigation of the relaxation trajectories showed that often bond rearrangements happen in the a-C-part of X during the relaxation which can be energetically favorable. Indeed, independent quantum molecular dynamics calculations of diamond with water suggest that such bond rearrangements can also be triggered by sliding of carbon surfaces lubricated with gas molecules.[10]

One aspect to consider is whether the local structure relaxations are sufficient to sample realistic final states X since local relaxation algorithms typically only proceed downhill in energy and cannot overcome energy barriers. Nevertheless, we see many fragmentation
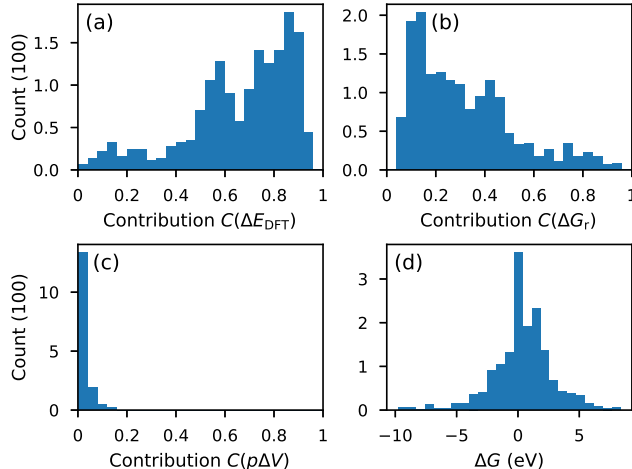
FIG. 6. (Color online) (a) Histogram of absolute contribution $C(\Delta E_{\mathrm{DFT}})$ to the Gibbs free energy (see main text). (b) same for $C(\Delta G_{\mathrm{r}})$. (c) same for $C(p\Delta V)$. (d) Histogram of Gibbs free energy values.

events of the molecules and the aforementioned bond-rearrangements in the a-C networks. This could be due to the fact that the automatically generated initial states used for the structure relaxations of X can deposit a substantial amount of potential energy in the system such that also rearrangements that would normally have a barrier (for instance when a molecule approaches an open pore from far away) can occur by only going downwards in energy from these initial configurations. In order to quantify this effect, we have analyzed, how ΔE_{DFT} is distributed before and after the structural relaxation. This is shown in Fig. 7 (a) (before structure optimization) and (b) (after structure optimization). Before the local structure optimization, the DFT energy of X is on average 7.26 eV higher and never lower than the sum of the a-C and M DFT energies. After the structure optimization, the mean value of ΔE_{DFT} is 0.01 eV.

Now that we have gained an overview of the sampled final states (products), in a next step, we calculate equilibrium concentrations of the possible products X at given total pressure, given partial pressures of the molecules in the gas phase and a given temperature. These equilibrium concentrations measure, how easily a certain molecule is chemisorbed to the a-C pores and possibly undergoes fragmentation. For this purpose, we now fix the initial a-C mass density and focus on the according representative a-C sample with $N = 128$ a-C atoms $C_1, \ldots, C_N$ inside the volume $V(\text{a-C})$. We treat these carbon atoms as different
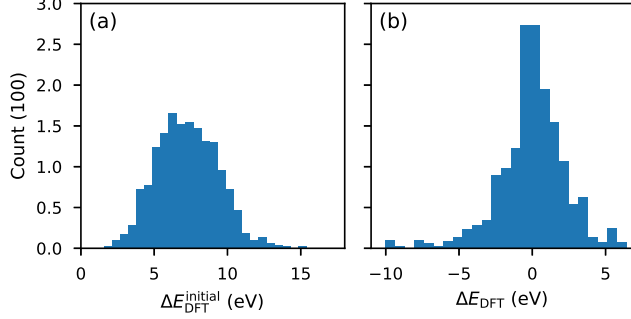
19

FIG. 7. (Color online) (a) Histogram of DFT energy difference $\Delta E_{\mathrm{DFT}}^{\mathrm{initial}}$ before optimizing the X structures. (b) Histogram of DFT energy difference ΔE_{DFT} after local geometry optimization.

chemical species, as they all exhibit a different local environment and we search for thermal equilibrium under the constraint that the a-C stays intact up to local changes near the interaction sites. In addition, we have five possible molecules M and many possible chemisorbed or fragmented final states $X_1, \ldots, X_k$ derived from the selected representative sample. We do not consider the isolated final states in the concentration analysis. For a given final state X_i, let $C_{\alpha_1^i}, \ldots, C_{\alpha_{l_i}^i}$ be the l_i unique a-C atoms in the connectivity graph of X_i (see section II D) and M_i the molecule involved in the reaction. We then have to equilibrate the k reactions

$$C_{\alpha_1^i} + \cdots + C_{\alpha_{l_i}^i} + M_i \rightleftharpoons X_i, \qquad i = 1, \ldots, k. \tag{11}$$
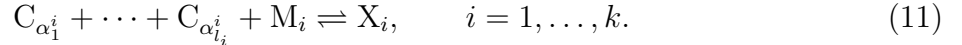
The total number of each carbon atom $C_1, \ldots, C_N$ has to be conserved (one carbon atom per sample for each C_m). This conservation leads to a competition for common a-C carbon atom reactants among different molecules or molecular fragments, which is the reason why a complete sampling — in the sense that every initial adsorption site is explored — is necessary.

Introducing the equilibrium constants[59] $K_1, \ldots, K_k$, the complex equilibrium is described by the non-linear system of $k + N$ equations

$$0 = \Delta G_i + k_{\mathrm{B}} T \ln K_i, \qquad\qquad\qquad i = 1, \ldots, k \tag{12}$$

$$0 = \frac{1}{V(\mathrm{a\text{-}C})} - c^{\mathrm{eq}}(C_m) - \sum_{i \in B_m} c^{\mathrm{eq}}(X_i), \qquad m = 1, \ldots, N \tag{13}$$

with the $k + N$ equilibrium concentrations $c^{\mathrm{eq}}(X_i)$ and $c^{\mathrm{eq}}(C_m)$ as unknown variables and

$$B_m = \left\{ i \in \{1, \ldots, k\} \,|\, m \in \{\alpha_1^i, \ldots, \alpha_{l_i}^i\} \right\}. \tag{14}$$

20

Here ΔG_i are the Gibbs free energy changes calculated from DFT simulations for the reference state with given total pressure, given partial pressures of the gas phase molecules, given temperature and reference concentrations $c(X_i) = \frac{1}{V(X_i)}$ and $c(C_{\alpha_j^i}) = \frac{1}{V(\text{a-C})}$ with $V(X_i)$ the volume of the relaxed simulation cell of the final state X_i. For the derivation of the a-C atom number conservation equations (13), we have assumed that the equilibrium mass density of the a-C atoms is conserved at $\frac{N}{V(\text{a-C})}$. This is justified, as $0.97 \leq \frac{V(X_i)}{V(\text{a-C})} \leq 1.03$ holds for all i and all of the four representative samples, and we assume that volume changes cancel out on average.

As our definition of the reference state depends on (partial) pressure and we have constant (partial) pressure in the NpT-ensemble (we assume an infinite gas phase reservoir), the activities of the gas phase molecules are always unity[59]. For the activities of the a-C atoms and the final states in equilibrium, we assume that they are given as concentration ratios of the form $a^{\text{eq}}(A) = \frac{c^{eq}(A)}{c(A)}$ for A any a-C atom or final state which means that different final states do not interact with each other apart from the contest for common reactants. Thus the equilibrium constants are given by

$$K_i = \frac{V(X_i) c^{\text{eq}}(X_i)}{V(\text{a-C})^{l_i} \prod_{j=1}^{l_i} c^{\text{eq}}(C_{\alpha_j^i})}. \tag{15}$$

Note that our choice of the reference state is not the standard state but rather given by the conditions of each of the DFT simulations and the choice of the gas phase reservoir, such that the K_i are not the standard equilibrium constants and the activities are not with respect to the standard state.

Not considering errors in ΔG_i due to approximations in the DFT calculations or chemical interactions between products, we expect that the calculated concentrations are slightly overestimated as the steric effect is underestimated by only taking the occupation of the bound a-C atoms into account (in reality, a fragment might block another a-C atom it is not bound to). We propose that those additional steric effects could be considered properly within our framework by introducing a virtual reactant for any pairwise spatial collision of final states. In this way, also a common analysis of isolated and chemisorbed/fragmented final states could be possible (isolated final states do not have carbon atoms as reactants and we therefore cannot describe them with our approach). We have however not followed this Ansatz within the current work in favor of simplicity. On the other hand, interactions between final states might lead to synergetic effects and thus to higher concentrations. All

21

in all, the absolute numbers of the calculated concentrations are not expected to be directly comparable to an experimental situation. Due to our large sampling pool, we however anticipate to be able to provide a qualitative description of the trends between the different molecules, the trends when altering the conditions of the gas phase reservoir and the trends when altering the a-C mass density.

In order to solve the high-dimensional system of non-linear equations numerically, we employ the following scheme, as straight-forward application of numerical root finding algorithms failed: First we automatically split the system in subsystems of mutually dependent equations. Equations depend on each other, if they (transitively) share common a-C atoms as reactants. Thus this splitting reduces the complexity. Then we solve every subsystem separately. For this purpose, we set all Gibbs free energy changes to zero and start with an initial guess for the equilibrium concentrations $c^{eq}(X_i) = c^{eq}(C_m) = \frac{1}{2V(a\text{-}C)}$. Then we solve the subsystem with a standard numerical root finding procedure (`scipy.optimize.root` with the Levenberg-Marquardt method[60]). We use the resulting concentrations as the initial guess for another run of the root finding algorithm with scaled down Gibbs free energy changes $\beta \Delta G_i$, $0 < \beta \leq 1$. We repeat this procedure, slowly increasing β linearly, until we reach $\beta = 1$ and thus obtain a solution for the true Gibbs free energy changes. Typically 10 to 20 steps for β are enough to find a solution. In order to exclude negative concentrations in the numerical solution, we use logarithmic concentrations as unknown variables. At the end of the procedure, residuals of the equations are checked to ensure that a proper solution has been found.

We now discuss a few different conditions of the gas phase reservoir and the resulting concentrations of the chemisorbed or fragmented molecules in the a-C.

C. Moist air

We start with moist air at $p = 10^5$ Pa. We use the following partial pressures for this condition: $p_{N_2} = 7.67 \cdot 10^4$ Pa, $p_{O_2} = 2.06 \cdot 10^4$ Pa, $p_{H_2O} = 1.76 \cdot 10^3$ Pa, $p_{CO_2} = 3.93 \cdot 10^1$ Pa and $p_{H_2} = 5.40 \cdot 10^{-2}$ Pa, which corresponds to a relative humidity of 50 % at 300 K. The five partial pressures do not sum up exactly to the total pressure, as we do not consider all components of air (for instance no noble gases). The resulting number concentrations of the
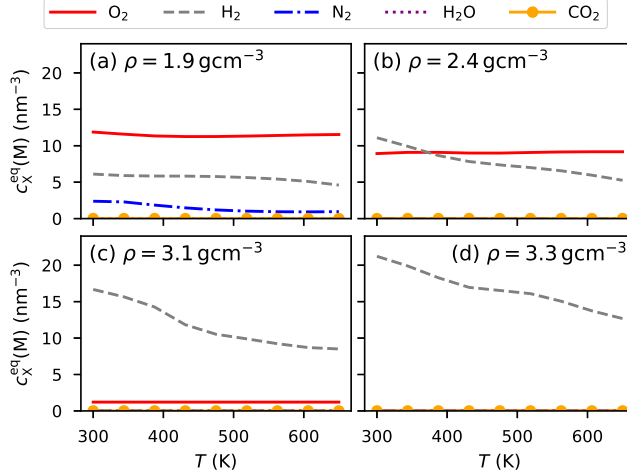
FIG. 8. (Color online) Equilibrium number concentrations $c_X^{eq}(M)$ of the chemisorbed or fragmented molecules for moist air at $p = 10^5$ Pa as a function of temperature. (a) – (d) representative samples 1 to 4 with different mass densities.

chemisorbed or fragmented molecules

$$c_X^{eq}(M) = \sum_{\substack{i \\ M=M_i}} c^{eq}(X_i) \tag{16}$$

are plotted in Fig. 8 (a) – (d) as a function of temperature for the four representative samples of different mass density.

For the chosen conditions, chemisorbed or fragmented O_2, H_2 and N_2 molecules are found in the a-C sample with the lowest mass density (Fig. 8 (a)). O_2 is most dominant, followed by H_2 and N_2. O_2 and H_2 concentrations are almost constant over the investigated temperature range. The N_2 concentration significantly drops with increasing temperature. Also chemisorbed or fragmented N_2 is only found in the sample with the lowest mass density. Chemisorbed or fragmented H_2O or CO_2 molecules are not present in any of the a-C samples. There are however many final states with isolated water or CO_2 in the pores which have been excluded from the analysis for simplicity.

For the second a-C sample with higher mass density (Fig. 8 (b)), the O_2 and H_2 concentrations are similar in magnitude. The H_2 concentration drops with increasing temperature while the O_2 concentration stays almost constant. For the two a-C samples with highest mass densities (Fig. 8 (c) and (d)), the pores are so small that basically only H_2 fits inside (compare Fig. 3). Consequently, only a high H_2 concentration is found. A small amount of
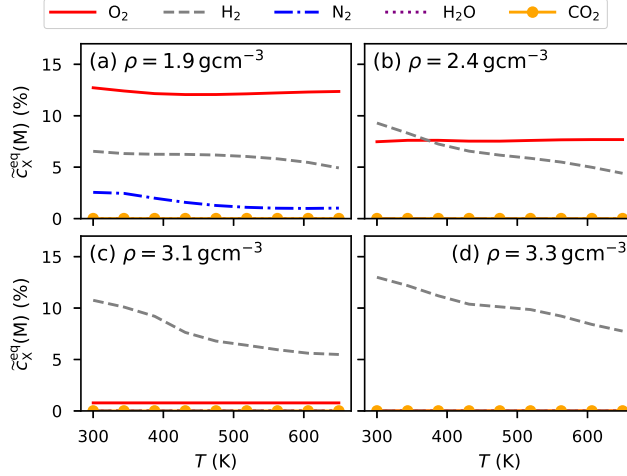
FIG. 9. (Color online) Same as Fig. 8 (a) – (d) except that concentrations are given as number per a-C atom. 100 % correspond to one molecule per a-C atom in the sample.

O_2 is still present in the largest pores of the a-C sample with second highest mass density. A similar temperature dependence is found for H_2 as in Fig. 8 (b). In general, there is the trend that H_2 concentration rises with increasing a-C mass density. In order to discriminate the effect of increasing reactant concentration with increasing a-C mass density from other effects, we switch from number concentration to number per a-C carbon atom. We denote those dimensionless concentrations with a tilde over the respective number concentration:

$$\tilde{c} = c\frac{V(\text{a-C})}{N} \tag{17}$$

with c any number concentration, $V(\text{a-C})$ the volume of the according representative sample and N the number of carbon atoms in the sample ($N = 128$). In other words: $\tilde{c}$ is the activity with the imaginary reference state that every a-C atom in the representative sample is occupied by one entity of interest on average, which would correspond to $\tilde{c} = 100$ %. Fig. 9 shows these activities derived from the concentrations from Fig. 8. For the remaining discussion, we stick to using the dimensionless concentrations instead of the number concentrations.

Switching to dimensionless concentrations, the trend of increasing H_2 concentration with increasing a-C mass density has almost vanished. Thus we can attribute this effect solely to the increased reactant concentration that comes with higher mass density. Still the H_2 concentration for lower temperatures is smaller for the lowest mass density compared to the other mass densities, which is due to competition with O_2 and the low partial pressure of
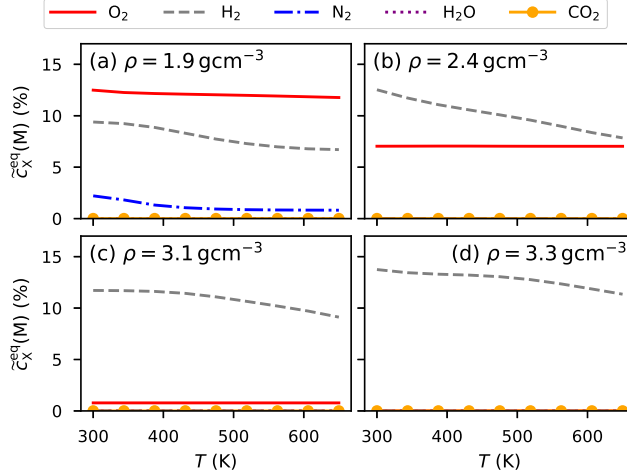
24

FIG. 10. (Color online) Same as Fig. 9 (a) – (d) except that the partial pressures are all set to $\frac{p}{5}$.

H_2 as we will see in a moment.

In summary, chemisorbed or fragmented O_2 is present irrespective of temperature whenever the pores are big enough. The H_2 concentration significantly decreases with increasing temperature. This is an interesting observation in the context of tribology as a-C loaded with hydrogen can act as a hydrogen source at elevated temperatures. Hydrogen is known to be able to cause corrosion in various metals and steel.[61]

D. Equal partial pressures

Although the partial pressure of H_2 is relatively low ($p_{H_2} = 5.40 \cdot 10^{-2}$ Pa) compared to the other molecules, there is a significant concentration of chemisorbed or fragmented H_2 molecules to be found in thermodynamic equilibrium. In order to understand the effect of partial pressure on the concentrations, we now consider a hypothetical ideal gas mixture with equal partial pressures $p_M = \frac{p}{5}$ for all the five molecules at $p = 10^5$ Pa. As always, the partial pressure of water is reduced to maintain equilibrium with the liquid phase whenever liquid water can exist. The resulting dimensionless concentrations are plotted in Fig. 10.

The H_2 concentrations for the different a-C mass densities now all look very similar and the temperature dependence is less pronounced. The concentrations for the other molecules are not much affected. All in all, partial pressure has a minor influence through a slightly altered chemical potential of the gas phase molecules. The most dominant part of ΔG_i is however in most cases the change in the DFT energy. Thus the actual composition of the
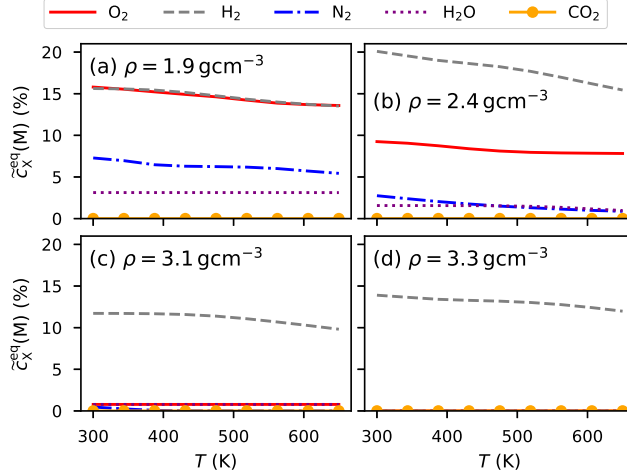
FIG. 11. (Color online) Same as Fig. 9 (a) – (d) except for pure gases (partial pressures are set subsequently to $p_M = p$ for all molecules).

gas is not so important for the scenario of thermodynamic equilibrium as long as all the molecules are present. The situation might be different when reaction barriers are taken into account in a more realistic non-equilibrium scenario or when a finite gas phase reservoir is considered.

E. Pure gases

In order to explore the effect of the competition for common reactants among the different gas molecules we now turn our attention to pure ideal gases (water still being in equilibrium with the liquid phase when possible). We thus solve the system of equations five times with $p_M = p = 10^5$ Pa for each of the five molecules and $p_M = 0$ for all other molecules. The resulting dimensionless concentrations are shown in Fig. 11.

In general, all concentrations are increased as compared to the situation of a mixture with equal partial pressure (note the slightly different scale compared to Fig. 9 and Fig. 10). The five-fold increase in partial pressure should only have a minor effect, as we have already seen. The major difference is that for pure gases, the effect of competition between different molecules is now missing. This effect is most severe for H_2O and N_2 which are less reactive than H_2 and O_2. Especially for the case of water, the concentration of fragmented or chemisorbed H_2O molecules is now non-vanishing (when the pores are big enough to accommodate H_2O). Thus the absence of chemisorbed or fragmented water in the scenario of
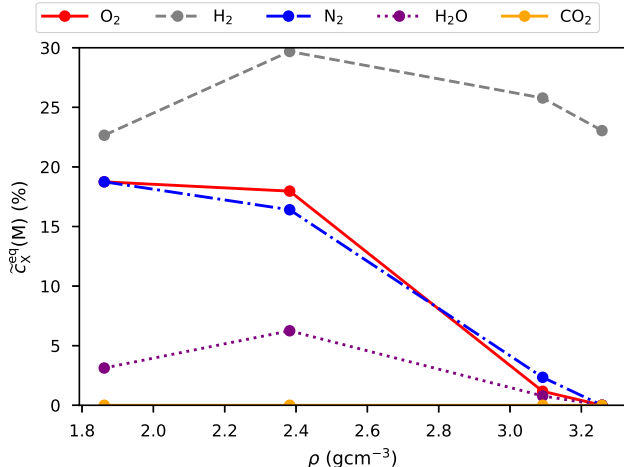
FIG. 12. (Color online) Upper limits ($\frac{\Delta G_i}{k_{\mathrm{B}}T} = -\infty$) for the dimensionless concentrations of pure gases as a function of a-C mass density.

moist air in thermodynamic equilibrium is due to the fact that all reactant carbon atoms are occupied by more reactive molecules. For pure CO_2, the concentration of chemisorbed or fragmented CO_2 is still zero, which is due to the fact that all 60 final states for CO_2 are found to be isolated.

Another interesting Gedankenexperiment is to set all Gibbs free energy changes to $\frac{\Delta G_i}{k_{\mathrm{B}}T} = -\infty$ for the pure gases, yielding an upper limit for the concentrations independent of pressure and temperature. By doing so, only the availability of suitable reactants limits the concentrations. Those upper limits are shown in Fig. 12.

Due to its small size, H_2 has the highest upper boundary for the concentration of chemisorbed or fragmented final states. This size effect is especially evident for the two samples with highest mass density where all other molecules show a very low upper boundary. The change in the upper limit for H_2 with a-C mass density falls within the variance expected from the finite size of the samples. In terms of at.% (number of H atoms per total C and H number of atoms), the upper limit found for hydrogen is about 35 at.% which is below the upper end of the range of experimentally found hydrogen content in hydrogen containing a-C (a-C:H) (30 at.% to 50 at.%)[2]. For the true ΔG_i values, the hydrogen concentration is further reduced compared to our upper limit. There are two main reasons why we find a lower H concentration than typical for a-C:H: First of all, this is expected as we start from pristine a-C where no hydrogen was available during the formation of the

27

network. It is therefore expected that some of the carbon-carbon bonds will never break up again to incorporate hydrogen into the network during local structure relaxation. In the experimental preparation of a-C:H, hydrogen is present already during the formation of the network. Secondly, we only consider reactions of the type $H_2 + \text{a-C} \rightarrow X$ but not $H_2 + X \rightarrow X'$ which produces mainly CH groups and leads to an underestimation of the occurrence of CH_2 groups as we will see in the analysis of reactants and chemical groups section.

The upper limits for O_2 and N_2 are practically identical, thus the differences in concentration in the more realistic scenarios arise from the true differences in ΔG_i. Although the size of H_2O is similar to O_2 and N_2 as judged by the radius R_M, the upper boundary for H_2O is substantially smaller. We attribute this to the fact that many of the H_2O final states are isolated and not fragmented or chemisorbed (H_2O only has 47 fragmented or chemisorbed final states in total compared to 134 for N_2 and 223 for O_2). Similarly, for CO_2 all final states are isolated, thus the upper boundaries are all zero.

Comparing Fig. 11 and Fig. 12, it is evident that O_2 and H_2 are quite reactive in the sense that a good part of the upper limit of the concentration is reached with the true ΔG_i values. N_2 is less reactive due to higher ΔG_i values. H_2O is less reactive both due to lower ΔG_i values and due to the fact that only a few initial configurations lead to a chemisorbed or fragmented final state. CO_2 only fits in the largest pores of the sample with lowest mass density and always shows an isolated final state.

F. The effect of total pressure

In the following, we restrict the discussion to moist air and pure water vapor (in equilibrium with liquid water) which appear to us as important scenarios within the tribological context. We now fix the temperature at $T = 400$ K and vary the total pressure from the ultra-high vacuum regime up to $p = 0.5$ GPa (a typical local pressure in tribological systems). It is of course questionable whether those peak pressures also prevail in the gas reservoir or only in the solid phase. Nevertheless we study those extreme pressure regimes to detect their possible effects. The tabulated experimental data for the chemical potential of real water ends at $p = 0.5$ GPa.[55] We thus did not consider higher pressures. Below $p = 10^5$ Pa, we treat H_2O as an ideal gas without the liquid phase, as below this pressure,
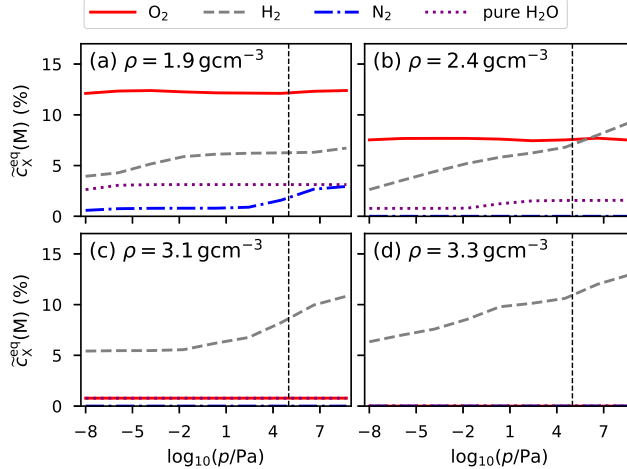
FIG. 13. (Color online) Dimensionless equilibrium concentrations of the chemisorbed or fragmented molecules for moist air and pure water at $T = 400$ K as a function of total pressure p (logarithmic pressure scale). (a) – (d) representative samples 1 to 4 with different mass densities. Dashed vertical line: $p = 10^5$ Pa.

no experimental data is available in our chosen source.[55] Due to the choice of temperature, no liquid water exists below $p = 10^5$ Pa anyway, such that this is not an issue.

Figure 13 displays the pressure dependence of the dimensionless concentrations of the chemisorbed or fragmented molecules for moist air (only O_2, H_2 and N_2 are non-vanishing) and pure water in the range $p = 10^{-8}$ Pa to $5 \cdot 10^8$ Pa. The O_2 concentration is independent of total pressure. The high pressure regime does not differ substantially from the $p = 10^5$ Pa results (dashed vertical line). The H_2 and N_2 concentrations slightly increase when going from 10^5 Pa to 0.5 GPa.

Even under ultra-high vacuum conditions ($p \leq 10^{-7}$ Pa), a considerable amount of chemisorbed or fragmented molecules are found in the a-C samples. The reason is that some of the adsorption sites are so reactive that the change in the chemical potential of the molecules due to total pressure is still not compensating the very low ΔE_{DFT} values. Additionally, we always consider an infinite gas phase reservoir which can never get depleted. In the case of pure water vapor, the concentration of chemisorbed or fragmented water is found to be practically constant with a decreasing concentration only in the vacuum regime.

In conclusion, the direct influence of total pressure of the gas phase reservoir on the concentrations is relatively low. The gas phase reservoir is however not the only entity

29

affected by a pressure change in a realistic situation: The density of the a-C phase formed during asperity collisions might be pressure dependent[62], leading to a dramatic change in the concentrations. Furthermore, in a non-equilibrium situation, pressure might also affect reaction barriers.

G.   Analysis of reactants and chemical groups

We now analyze the reactivity of the different kinds of carbon atoms (differentiated by coordination and dangling bond) as well as the chemical groups that are formed by the chemisorbed molecules and their fragments. As we have seen in the previous sections, we can safely restrict the conditions to $p = 10^5$ Pa and $T = 300$ K without loss of generality. Again we focus on air and pure water. Figure 14 shows the dimensionless concentrations $\tilde{c}_{\text{C}}$ of the different kinds of carbon atoms in the pristine a-C and the dimensionless concentrations of the occupied carbon atoms after reacting with the gas molecules for (moist) air and pure water $\tilde{c}_{\text{C}\,\text{occ}}^{\text{eq}}$ which are calculated as

$$\tilde{c}_{\text{C}}(K) = \frac{1}{N} \sum_{\substack{m=1 \\ \text{kind}(\text{C}_m)=K}}^{N} 1 \qquad \text{and} \tag{18}$$

$$\tilde{c}_{\text{C}\,\text{occ}}^{\text{eq}}(K) = \tilde{c}_{\text{C}}(K) - \frac{V(\text{a-C})}{N} \sum_{\substack{m=1 \\ \text{kind}(\text{C}_m)=K}}^{N} c^{\text{eq}}(\text{C}_m), \tag{19}$$

where the kind K is one of c2, c2*, c3, c3* or c4 corresponding to 2-fold coordinated without dangling bond, 2-fold coordinated with dangling bond, and so on. The coordination and dangling bond property are determined in the pristine a-C before the reaction has happened.

Judged by absolute numbers, most of the occupied a-C atoms are 3-fold coordinated atoms without dangling bonds except for the sample with highest mass density, where most of the occupied a-C atoms are 4-fold coordinated atoms without dangling bonds. In order to get a measure for the reactivity of the different kinds of carbon atoms, we have plotted the relative occupations $\tilde{c}_{\text{C}\,\text{occ}}^{\text{eq}}(K)/\tilde{c}_{\text{C}}(K)$ in Fig. 15.

It is evident, that c2, c2* and c3* carbon atoms are most reactive, followed by c3. Carbon atoms with a dangling bond are up to twice as reactive as carbon atoms with the same coordination but without dangling bonds. Atoms with 4 nearest neighbors are clearly occupied less frequently by gas molecules or fragments thereof. The reason why pure water did not
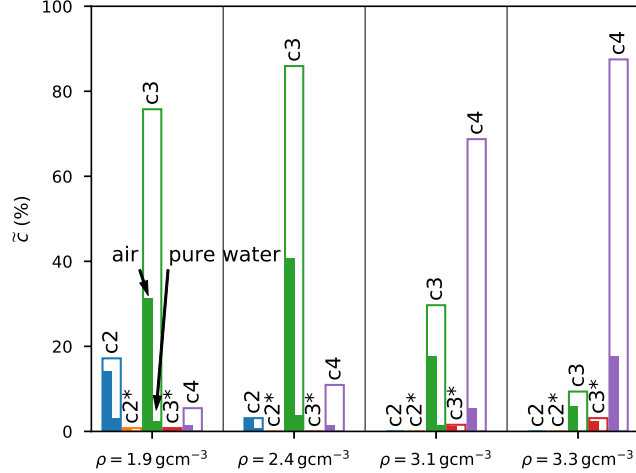
FIG. 14. (Color online) Occurrence ($\tilde{c}_C(K)$, hollow bars) and occupation ($\tilde{c}_{C\,occ}^{eq}(K)$, left solid bars: air, right solid bars: pure water) of the a-C atoms in the four representative samples. cn: n-fold coordinated a-C atom. *: with dangling bond. 100 % correspond to all atoms in the sample. Coordination and dangling bonds refer to pristine a-C before the reaction with gas molecules.

react with some of the atoms with dangling bonds at all could be that water needs several reactants to split. When the local environment of the atoms with dangling bonds is not in favor of splitting or adsorbing water, an isolated final state is found, which does not enter our analysis.

Although the scenario of thermodynamic equilibrium could be far from the conditions during an actual asperity collision, we expect that the increase in reactivity between carbon atoms without and with a dangling bond is universal. The formation of a-C dangling bonds due to mechanical load in a tribological context is thus a possible source of increased reactivity with ambient gases. In order to see, which molecules preferentially react with dangling bonds, and which chemical groups are formed, we now analyze the fragments of our reactions as described in section II D.

In total, we have found 20 different fragments and identified the corresponding chemical groups. The graphs along with the associated names of the chemical groups are listed in Table SM3 of the Supplemental Material[36]. The dimensionless concentration of a chemical group G in equilibrium is then given by

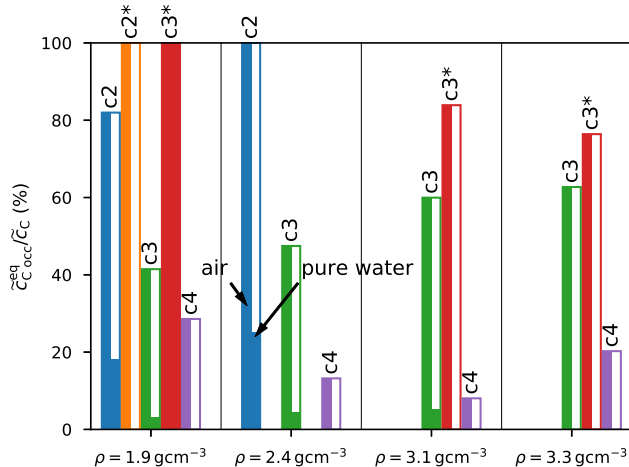$$\tilde{c}_F^{eq}(G) = \sum_{i=1}^{k} g(X_i, G)\tilde{c}^{eq}(X_i) \tag{20}$$

31

FIG. 15. (Color online) Same as Fig. 14 except that the relative occupations $\tilde{c}^{\mathrm{eq}}_{\mathrm{C\,occ}}(K)/\tilde{c}_{\mathrm{C}}(K)$ are plotted. Data points with $\tilde{c}_{\mathrm{C}}(K) = 0$ are omitted (no label for the atom kind is drawn). Hollow bars are just a guide to the eye to discriminate air and pure water data points. 100 % correspond to all available atoms of a certain kind being occupied in equilibrium.

with $g(\mathrm{X}_i, G)$ the number of fragments in final state X_i which are classified as chemical group G. The dimensionless equilibrium concentrations of the chemical groups found in the four representative a-C samples in contact with (moist) air are shown in Fig. 16. For each a-C sample, we have only plotted the most important chemical groups which constitute 99 % of $\sum_G \tilde{c}^{\mathrm{eq}}_{\mathrm{F}}(G)$. Furthermore, the most important reactant combinations are plotted for each group. Here we have also used a cutoff of 99 % of the cumulative contribution. The notation for the reactant combinations is M N_1 K_1 N_2 K_2 $\cdots$ where M denotes the molecule involved in the reaction and N_i is the number of a-C atoms of kind K_i. For example "O_2 2c2 c3" means that a certain chemical group is found as one of the fragments of a reaction of an oxygen molecule with two 2-fold coordinated a-C atoms and one 3-fold coordinated a-C atom.

The variety of chemical groups decreases with increasing a-C mass density which can be attributed to the decrease of c2 content as well as the decreasing pore size. Furthermore we find that there are no chemisorbed hydrogen molecules: All hydrogen molecules are dissociated and found as CH groups. Some of the final states also show CH_2 groups. The concentration is however so small that it falls out of the 99 % cutoff. The absence of CH_2 groups is certainly due to the approximation that we only consider reactions of the type
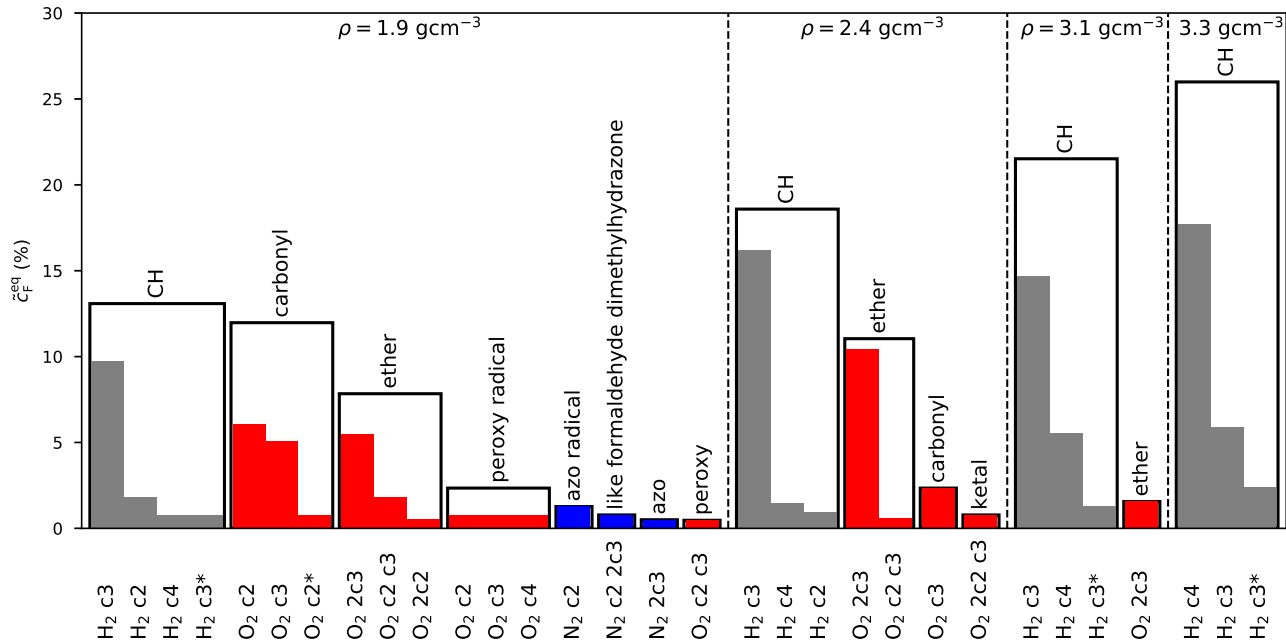
32

FIG. 16. (Color online) Hollow bars: dimensionless equilibrium concentrations of chemical groups for the four representative a-C samples in contact with air at $T = 300$ K and $p = 10^5$ Pa. Filled bars: contributions of different reactant combinations leading to the same group. Color by molecule: gray: H_2, red: O_2, blue: N_2. 100 % correspond to one group per a-C atom.

$M + a$-$C \rightarrow X$ but not $M + X \rightarrow X'$. For the same reason we do not see hydroxyl groups. These errors could be corrected within our analysis framework by considering additional reactions with the most abundant final states as new initial states. For the sake of simplicity, we have however refrained from considering such multi-step reactions. For the CH group, the dominant a-C kind is c3 except for the highest mass density, where c4 takes over. Nitrogen is only found when a 2-fold coordinated a-C atom is involved with the exception of the azo group. The most common group for nitrogen is an azo radical.

The most important groups involving oxygen are carbonyl (C=O) and ether (C-O-C). Carbonyl dominates in the low density sample and is preferentially found when 2-fold coordinated a-C atoms are available. Already for the second mass density, the ether group is far more dominant than carbonyl as 2-fold coordinated atoms become less available. The less abundant groups containing oxygen are peroxy radical, peroxy and ketal. Dangling bonds are mainly found in reactants leading to the CH group and to a lower extent also carbonyl.

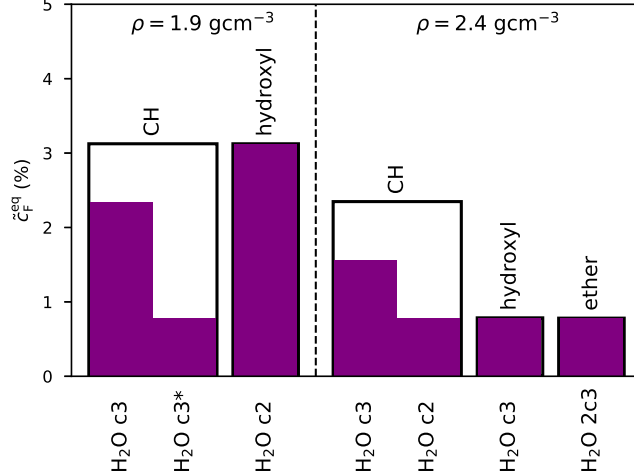The group and reactant analysis for a-C in contact with pure water is shown in Fig. 17,

33

FIG. 17. (Color online) Same as Fig. 16 but for pure water.

where we have only shown the two lowest mass densities since no final states involving water are expected for the two samples with high mass density as can be seen from Fig. 12. Water splitting events either lead to a hydroxyl and a CH group or to an ether and two CH groups. Again a-C atoms with a dangling bond undergoing a reaction are saturated by forming CH groups.

IV. CONCLUSION

We have conducted an ab initio thermodynamics study to investigate the reaction of amorphous carbon of different mass densities with ambient gas molecules. DFT simulation have been performed to sample Gibbs free energy changes of a large number of reactions covering all initial adsorption sites, enabling us to calculate equilibrium concentrations of chemisorbed and fragmented final states. Our analysis takes into account the competition for common a-C atoms as reactants between the five gas molecules O_2, H_2, N_2, H_2O and CO_2. The investigated representative a-C samples differ by coordination numbers of the a-C atoms, occurrence of dangling bonds and pore size. In general, we have observed that the specific conditions (temperature, total pressure, partial pressures) of the gas phase reservoir often play only a subordinate role in thermodynamic equilibrium. The concentrations of chemisorbed or fragmented molecules are mainly governed by the availability and accessibility of a-C sites with a reactive local environment and the competition among molecules. An interesting outcome of our analysis is that in thermodynamic equilibrium, no products

34

of chemisorbed or fragmented water are found for the case of moist air. This could be traced back to the competition for common a-C atoms as reactants with the more reactive molecules O_2 and H_2 and the preference of water to form physisorbed instead of chemisorbed or fragmented final states. Only in the case of pure water vapor, water dissociation is observed.

In summary, first steps towards the microscopic understanding of the interaction of amorphous carbon formed during a tribological contact of diamond (like) carbon coatings with ambient gases have been taken. The scenario of thermodynamic equilibrium is certainly a severe approximation for the conditions of an asperity collision which can be governed by kinetic effects and mechanochemistry[12,16]. Nevertheless, we believe that a knowledge about equilibrium concentrations of reactants and products provide interesting complementary information to large scale quantum molecular dynamics calculations of tribo-induced reactions[10,16]. Indeed, we have found a few observations which we believe are universal in the sense that they can be transferred to non-equilibrium situations: For example the role of dangling bonds, the temperature dependence of the hydrogen concentration and the switching from carbonyl to ether groups with increasing a-C mass density.

In this work we have also developed a toolchain that allows to calculate equilibrium concentrations of competing reactions in amorphous materials from ab initio principles. These concepts can easily be transferred to study for example amorphous surfaces in contact with gas mixtures. Possible extensions of our work are the inclusion of multi-step reactions and the common analysis of chemisorbed, fragmented and isolated (physisorbed) final states by introducing virtual reactants accounting for spatial collisions of products which do not form chemical bonds.

HFR04.

---

[*] michael.moseler@iwm.fraunhofer.de

[1] O. A. Williams, Diam. Relat. Mater. **20**, 621 (2011).

[2] J. Robertson, Mater. Sci. Eng. R **37**, 129 (2002).

[3] A. Erdemir and C. Donnet, J. Phys. D **39**, R311 (2006).

[4] P. J. Kelly, R. D. Arnell, M. D. Hudson, A. E. J. Wilson, and G. Jones, Vacuum **61**, 61 (2001).

[5] A. V. Sumant, A. R. Krauss, D. M. Gruen, O. Auciello, A. Erdemir, M. Williams, A. F. Artiles, and W. Adams, Tribol. Trans. **48**, 24 (2005).

[6] S. C. Tung and H. Gao, Wear **255**, 1276 (2003).

[7] M. Kalin and J. Vižintin, Wear **259**, 1270 (2005).

[8] H. I. Kim, J. R. Lince, O. L. Eryilmaz, and A. Erdemir, Tribol. Lett. **21**, 51 (2006).

[9] M. Moseler, H. Riedel, P. Gumbsch, J. Stäring, and B. Mehlig, Phys. Rev. Lett. **94**, 165503 (2005).

[10] T. Kuwahara, G. Moras, and M. Moseler, Phys. Rev. Lett. **119**, 096101 (2017).

[11] L. Pastewka, M. Mrovec, M. Moseler, and P. Gumbsch, MRS Bull. **37**, 493 (2012).

[12] L. Pastewka, S. Moser, P. Gumbsch, and M. Moseler, Nat. Mater. **10**, 34 (2011).

[13] T. Kunze, M. Posselt, S. Gemming, G. Seifert, A. R. Konicek, R. W. Carpick, L. Pastewka, and M. Moseler, Tribol. Lett. **53**, 119 (2014).

[14] L. Pastewka, S. Moser, M. Moseler, B. Blug, S. Meier, T. Hollstein, and P. Gumbsch, Int. J. Mater. Res. **99**, 1136 (2008).

[15] G. Zilibotti, S. Corni, and M. C. Righi, Phys. Rev. Lett. **111**, 146101 (2013).

[16] A. Peguiron, G. Moras, M. Walter, H. Uetsuka, L. Pastewka, and M. Moseler, Carbon **98**, 474 (2016).

[17] J. R. Hird and J. E. Field, Proc. R. Soc. A **460**, 3547 (2004).

[18] M. Moseler, L. Pastewka, and J. Hird, "Taming the Untamable — The Art and Science of Diamond Polishing," in *Comprehensive Hard Materials*, Vol. 3 (Elsevier, 2014) pp. 81–98.

[19] A. R. Konicek, D. S. Grierson, P. U. P. A. Gilbert, W. G. Sawyer, A. V. Sumant, and R. W. Carpick, Phys. Rev. Lett. **100**, 235502 (2008).

[20] A. R. Konicek, D. S. Grierson, A. V. Sumant, T. A. Friedmann, J. P. Sullivan, P. U. P. A.

Gilbert, W. G. Sawyer, and R. W. Carpick, Phys. Rev. B **85**, 155448 (2012).

[21] M. Godet, Wear **100**, 437 (1984).

[22] Y. Berthier, M. Godet, and M. Brendle, Tribol. Trans. **32**, 490 (1989).

[23] D. A. Rigney and S. Karthikeyan, Tribol. Lett. **39**, 3 (2010).

[24] J. Fontaine, M. Belin, T. Le Mogne, and A. Grill, Tribol. Int. **37**, 869 (2004).

[25] C. Matta, L. Joly-Pottuz, M.-I. De Barros Bouchet, J. M. Martin, M. Kano, Q. Zhang, and W. A. Goddard, Phys. Rev. B **78**, 085436 (2008).

[26] M.-I. De Barros Bouchet, G. Zilibotti, C. Matta, M. C. Righi, L. Vandenbulcke, B. Vacher, and J.-M. Martin, J. Phys. Chem. C **116**, 6966 (2012).

[27] M.-I. De Barros Bouchet, C. Matta, T. Le-Mogne, J. M. Martin, Q. Zhang, W. Goddard, M. Kano, Y. Mabuchi, and J. Ye, J. Phys. Conf. Ser. **89**, 012003 (2007).

[28] J. A. Harrison, D. W. Brenner, C. T. White, and R. J. Colton, Thin Solid Films **206**, 213 (1991).

[29] O. Manelli, S. Corni, and M. C. Righi, J. Phys. Chem. C **114**, 7045 (2010).

[30] H. Tamura, H. Zhou, Y. Hirano, S. Takami, M. Kubo, R. V. Belosludov, A. Miyamoto, A. Imamura, M. N. Gamo, and T. Ando, Phys. Rev. B **62**, 16995 (2000).

[31] J. D. Schall, G. Gao, and J. A. Harrison, J. Phys. Chem. C **114**, 5321 (2010).

[32] L. Pastewka, P. Pou, R. Pérez, P. Gumbsch, and M. Moseler, Phys. Rev. B **78**, 161402(R) (2008).

[33] L. Pastewka, "Atomistica — Interatomic potentials library," http://www.atomistica.org/.

[34] E. Vanden-Eijnden and G. Ciccotti, Chem. Phys. Lett. **429**, 310 (2006).

[35] B. Cordero, V. Gómez, A. E. Platero-Prats, M. Revés, J. Echeverría, E. Cremades, F. Barragán, and S. Alvarez, Dalton Trans. , 2832 (2008).

[36] See Supplemental Material at (URL will be inserted by publisher) for details regarding the pore analysis, local magnetic moments of the model molecules, connectivity analysis, feature vectors and best representatives of virtual samples and connectivity graphs.

[37] J. C. Russ, *The Image Processing Handbook*, 4th ed. (CRC Press LLC, 2002).

[38] G. Kresse and J. Hafner, Phys. Rev. B **47**, 558(R) (1993).

[39] G. Kresse and J. Hafner, Phys. Rev. B **49**, 14251 (1994).

[40] G. Kresse and J. Furthmüller, Comp. Mater. Sci. **6**, 15 (1996).

[41] G. Kresse and J. Furthmüller, Phys. Rev. B **54**, 11169 (1996).

[42] J. P. Perdew, K. Burke, and M. Ernzerhof, Phys. Rev. Lett. **77**, 3865 (1996).

[43] J. P. Perdew, K. Burke, and M. Ernzerhof, Phys. Rev. Lett. **78**, 1396 (1997).

[44] P. E. Blöchl, Phys. Rev. B **50**, 17953 (1994).

[45] G. Kresse and D. Joubert, Phys. Rev. B **59**, 1758 (1999).

[46] T. Takeda, Z. Phys. B **32**, 43 (1978).

[47] A. Tkatchenko and M. Scheffler, Phys. Rev. Lett. **102**, 073005 (2009).

[48] T. Kerber, M. Sierka, and J. Sauer, J. Comput. Chem. **29**, 2088 (2008).

[49] E. Bitzek, P. Koskinen, F. Gähler, M. Moseler, and P. Gumbsch, Phys. Rev. Lett. **97**, 170201 (2006).

[50] A. H. Larsen, J. J. Mortensen, J. Blomqvist, I. E. Castelli, R. Christensen, M. Dułak, J. Friis, M. N. Groves, B. Hammer, C. Hargus, E. D. Hermes, P. C. Jennings, P. B. Jensen, J. Kermode, J. R. Kitchin, E. L. Kolsbjerg, J. Kubal, K. Kaasbjerg, S. Lysgaard, J. B. Maronsson, T. Maxson, T. Olsen, L. Pastewka, A. Peterson, C. Rostgaard, J. Schiøtz, O. Schütt, M. Strange, K. S. Thygesen, T. Vegge, L. Vilhelmsen, M. Walter, Z. Zeng, and K. W. Jacobsen, J. Phys.: Condens. Matter **29**, 273002 (2017).

[51] J. N. Harvey, Phys. Chem. Chem. Phys. **9**, 331 (2007).

[52] F. H. Allen, O. Kennard, D. G. Watson, L. Brammer, A. G. Orpen, and R. Taylor, J. Chem. Soc., Perkin Trans. 2 , S1 (1987).

[53] J. Rogal and K. Reuter, in *Experiment, Modeling and Simulation of Gas-Surface Interactions for Reactive Flows in Hypersonic Flights*, Educational Notes RTO-EN-AVT, Vol. 142 (2007) pp. 1–18, paper 2.

[54] D. Alfè, G. A. de Wijs, G. Kresse, and M. J. Gillan, Int. J. Quant. Chem. **77**, 871 (2000).

[55] M. Chase, *NIST-JANAF Thermochemical Tables*, 4th ed. (J. Phys. Chem. Ref. Data, 1998) Monograph 9.

[56] H. U. Jäger and K. Albe, J. Appl. Phys. **88**, 1129 (2000).

[57] "ChemSpider," http://www.chemspider.com/.

[58] L. Pisani, B. Montanari, and N. M. Harrison, Phys. Rev. B **80**, 104415 (2009).

[59] C. E. Mortimer and U. Müller, *Chemie*, 10th ed. (Thieme, 2010).

[60] E. Jones, T. Oliphant, P. Peterson, *et al.*, "SciPy: Open source scientific tools for Python," http://www.scipy.org/.

[61] S. Lynch, Corros. Rev. **30**, 105 (2012).

[62] J. von Lautz, L. Pastewka, P. Gumbsch, and M. Moseler, Tribol. Lett. **63**, 26 (2016).

[63] Jülich Supercomputing Centre, J. large-scale research facilities **4** (2018), 10.17815/jlsrf-4-121-1.